Oil-Water Transport in Clay-Hosted Nanopores: Effects of Long-Range Electrostatic Forces

Hao Xiong[1], Deepak Devegowda[1], and Liangliang Huang[2]

[1]University of Oklahoma Norman Campus
[2]University of Oklahoma

May 5, 2020

Abstract

Charged clay surfaces can impact storage and mobility of hydrocarbon and water mixtures. Here, we use equilibrium molecular dynamics (MD) and nonequilibrium MD simulations to investigate hydrocarbon-water mixtures and their transport in slit-shaped illite nanopores. We construct two illite pore models with different surface chemistries: potassium-hydroxyl (P-H) and hydroxyl-hydroxyl (H-H) structures. In H-H nanopore, we observe water adsorption on the clay surfaces. In P-H nanopores, however, we observe the formation of water bridges or columns between the top and bottom pore surfaces. This is because of the existence of a local, long-range electric field within the P-H pore causing water molecules to align in a specific direction promoting the formation of a water bridge. Our NEMD simulations demonstrate that the velocity profiles across the pore depends strongly on the presence or absence of the water bridge. This study provides a theoretical basis for understanding of nanofluidics with charged surfaces.

Introduction

The behavior of fluids confined in nanopores is crucial for understanding and resolving a suite of challenging problems such as nanofluidic technology[1], biochemical flows[2] and membrane separation[3]. The structure and dynamics of confined fluids differ drastically from those in bulk condition[4–9] as a result of interactions with the nanopore walls[10–12]. With charged surfaces, this effect can be more pronounced through the creation of electric double layer (EDL) structures [13,14] and the behavior of water in the EDL[15,16]. These phenomena merit a deeper look in to liquid transport through nanoporous structures with charged surfaces.

There have been several studies focusing on nano-confined fluid structures adjacent to charged surfaces. Urashima et al. discuss the structure of water at a negatively charge silica surface and demonstrate that the closest water molecules form hydrogen bonds with the negatively charged silica surface[17]. Dobrynin et al. investigate adsorption between a polyampholyte chain and a charged surface[18] while Zhang et al. demonstrate that the charged surface can regulate molecular orientation and interaction[19]. Tasca et al indicate that a positively charged surface can enhance electron transfer[20] and Dreier et al. state that the alignment and transport of water molecules are influenced by charged surfaces[21]. Ehre et al. conclude that water molecules freeze differently on positively and negatively charged surfaces[22] and Lahann et al. demonstrate that charged surfaces can switch interfacial properties, such as wettability in response to an electrical potential[23]. Lis et al. state that in addition to causing water alignment at the surface, the charged surface can lead to surface-charge screening[24].

These contributions enhance our understanding of fluid confinement within charged nanopore surfaces; however, a more complete picture should encompass a discussion of transport. Clay minerals are one of the

most fundamental and abundant substances on earth [25]and can be used as adsorbents[26], carbon dioxide storage and sequestration[27,28] as well as water purification[29]. Generally, clay minerals carry negative surface charges and nonbonded positive cations[30,31] creating negative and positively charged surfaces that make fluid transport quite complex[32]. There is also strong evidence that positive cations in the fluid can also influence both the structure and distribution of fluid[15,33–36].

Mixture flow in nanopores, such as flow of red blood cells[37], drug delivery[38] and oil and gas production from shales[39] are quite common. In our work, a dodecane and ethane mixture form the non-wetting hydrocarbon phase and water the wetting fluid phase[40–42]. We use equilibrium molecular dynamics (EMD) and nonequilibrium MD (NEMD) to investigate the structure and transport of hydrocarbon-water mixtures in clay-hosted nanopores with different charged surface chemistries.

Our paper is organized as following: Section 2 describes the construction of different clay models with varying surface chemistries and clay-hosted pores containing hydrocarbon-water mixtures in a molecular dynamics simulation setup. In total, this section discusses 42 MD simulations with varying pore size (5 nm, 10 nm and 15 nm), water concentration (0-100%) and surface charges. Section 3 provides a thorough analysis on fluid structure based on results from Section 2 and Section 4 discusses transport of the hydrocarbon-water mixture based on the results from Section 2 and 3. In Section 5, we show how the single-phase velocity profiles are different for P-H and H-H pores and finally, we present our conclusions in Section 6.

2. Models and Methodology

2.1 Structure of illite and charged surface chemistry

Kaolinite, illite, chlorite and smectite are the most commonly occurring clay minerals[43] with illite being the most common diagenetic product in shales[44]. Generally, clay-hosted pores in shales are slit-shaped or cylindrical, with few occurrences of oval- and cone- shaped pores[45,46]. Because slit pores are the most prevalent[47], we focus on investigating fluid transport in illite-hosted slit-shaped pores.

The chemical formula of illite is $K[Si_7Al](Al_4)O_{20}(OH)_4$, according to Zhang et al.[48]. Isomorphic substitutions in each unit cell of our model are made by replacing one Si^{4+} by one Al^{3+}. Loewenstein's rule is used for ion substitution in clay minerals so that the locations of two substitution sites are not adjacent to each other[49]. Interlayer cations (potassium cations, K^+) are placed randomly in the interlayer space of illite to counterbalance the electrostatic charges induced by the isomorphic substitutions. The K^+ cations can move in the interlayer space.

The simulation box contains 20 clay unit cells (forming a 10×2×1 supercell), with dimensions of 6.4042 nm×2.2308nm×1.0204 nm (x-, y- and z-direction) as shown in Fig. 1. The slit pore is constructed with four parallel illite layers confined in a three-dimensional simulation box. 2 illite layers form the top pore surface and the other two illite layers form the bottom. Each illite pore model has three different basal spacings (5nm, 10nm, and 15nm).

There are generally four illite slit pore structures discussed in literature based on charged clay surface chemistry: potassium-hydroxyl (P-H)[50], hydroxyl-hydroxyl (H-H)[51], potassium-potassium (P-P)[48], and a structure[52] between the P-H and H-H configurations. The corresponding illustrations are shown in the Fig.S-1 in Supporting Information. This work considers only the potassium-hydroxyl (P-H) and hydroxyl-hydroxyl (H-H) structures and a schematic of both are shown in Figs. 2a-b.

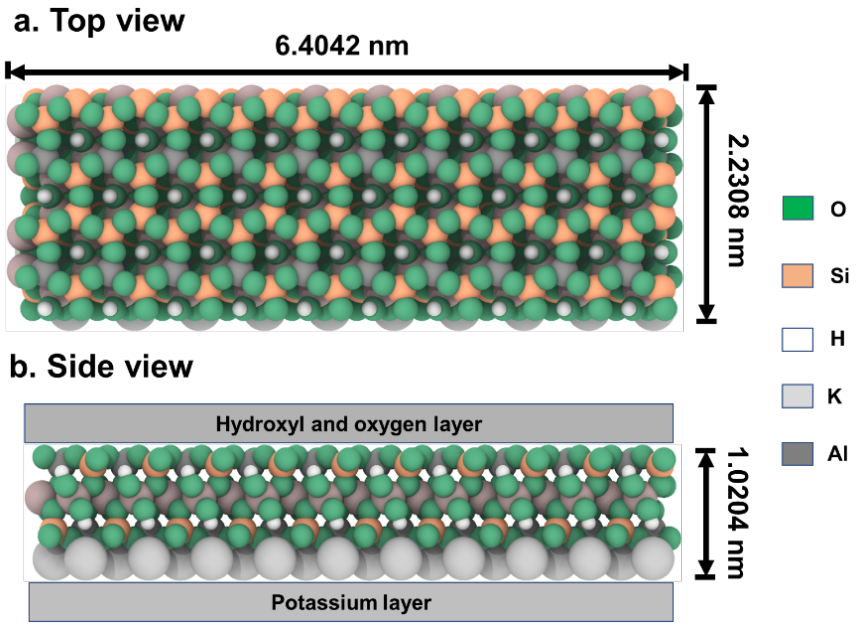

Fig. 1 Schematic representation of the illite supercell (10×2×1). The dimension is 6.4042 nm×2.2308 nm×1.0204 nm. Panels a and b provide top and side views of the illite supercell.

Color codes: O, green; Al, grey; H, white; Si, orange; K^+, light grey.

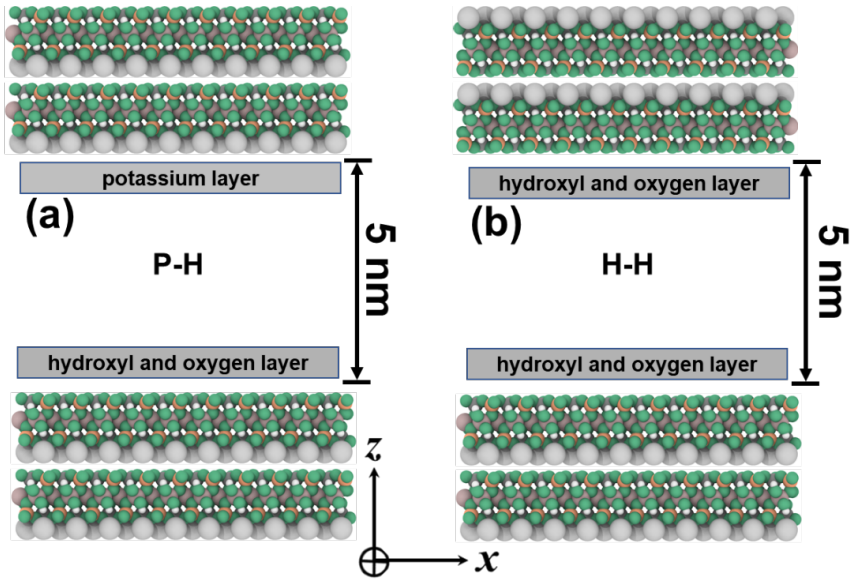

Fig. 2 Illustration of the illite-slit pore in potassium-hydroxyl (P-H) and hydroxyl-hydroxyl (H-H) configuration with a pore width of 5 nm. Color codes are as in **Fig.1** . The configurations with 10 nm and 15 nm pore width are not shown but are used in this study.

We construct seven models with different water concentrations for each of the three slit pore widths. Table S-1 in Supporting Information summarizes all the 21 P-H models. We construct 21 additional MD models

with the H-H configuration that are also listed in Table S-1. In the interests of space, we only show the initial configurations of the P-H models with a pore width of 5nm in Fig. 3.

The temperature and pressure are kept constant at 350 K and 400 atm. In order to keep pressure conditions similar across all models, an increase in water concentration is accompanied by a decrease in the number of hydrocarbon molecules.

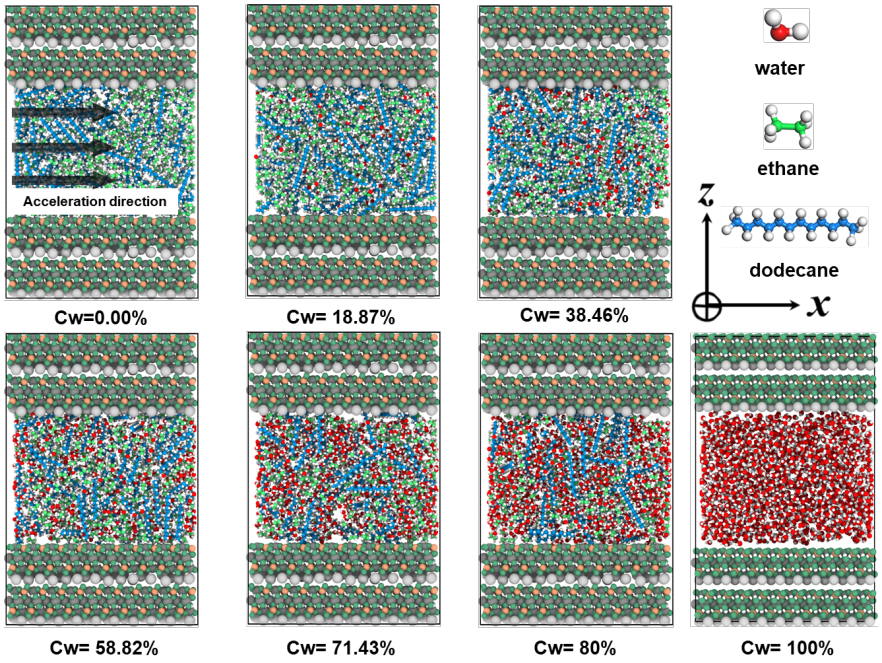

Fig. 3 Snapshots showing the initial configurations of the seven P-H slit pore models of 5 nm width with varying water concentration. Cw stands for the water concentration. The clay structure uses the same color codes as in **Fig. 1** . The color codes of fluid molecules are: ethane in light green; dodecane in light blue; and H_2O in red. In the first panel, the direction of the arrows indicates the direction of an imposed acceleration in subsequent sections of this paper.

2.2 Discussion of the Force Field

We apply the ClayFF force field to describe the interatomic interactions for illite and the cations[53] as is common with clay molecular simulations[54,55]. Water molecules are described using a flexible SPC model and the shake algorithm is used to make the two O-H bonds and the H-O-H angle rigid[56]. We use the OPLS All-Atom force field to represent the organic components (ethane and dodecane)[57]. We also use the Lorentz-Berthelot mixing rules to calculate the interaction parameters between unlike atoms. It should be noted that the mixing rules of ClayFF and OPLS All-Atom force fields are different. The OPLS All-Atom force field uses a geometric mixing rule to obtain the Lennard-Jones interaction parameters between unlike atoms[57], while the Lorentz-Berthelot mixing rule is used for ClayFF force field[53]. For the interaction parameters between clay and organic components, the use of Lorentz-Berthelot mixing rule has been documented in Hao et al.[50], Wu et al.[58], and Zhao et al.[59] for methane adsorption in clay minerals and is also applied in our study.

2.3 Simulation Details

We use the Large-scale Atomic/Molecular Massively Parallel Simulator (LAMMPS)[60] with periodic boundary conditions in all three directions with short-range interactions represented by a Lennard-Jones (LJ) 12-6 term.[61] The cutoff distance for the short-range nonbonded van der Waals interactions is 8 Å and the long-range electrostatic interactions are calculated by the Fourier-based Ewald summation method[62] - the particle-particle/particle-mesh (PPPM) method with a precision value of 10^{-6} [63].

Our workflow is as follows: In the initial set-up, hydrocarbon and water are placed randomly within the pores using the Packmol package[64]. We then run equilibrium MD (EMD) simulations using an NPT ensemble using a time step of 0.01 fs for 100ps and of 1 fs for the next 5 ns. Pressure is controlled at 400 atm by the Parrinello-Rahman barostat[65] while temperature is held at 350 K by the Nose Hoover thermostat [66]. With equilibrium in the NPT ensemble, we switch to the NVT ensemble and continue the simulations for another 5 ns.

After EMD simulations, non-equilibrium MD (NEMD) simulations are performed for another 10 ns to mimic hydrocarbon-water transport. Several methods exist for inducing flow in molecular dynamics, such as forced[67–69], surface-induced, pressure difference[70], osmotic pressure[71] and gravitational approaches[72–74]. In our simulations, we adopt the gravitational technique because other methods have been known to cause a distortion of the velocity-field and density profile along the flow direction[74–76]. A constant external gravity-like force, parallel to the basal plane (along the x-direction as shown in Fig. 3), is exerted on all hydrocarbon-water molecules inside the illite nanopores[77,78]. To ensure a linear system response, we maintain a constant acceleration of each particle on the order of 10^{-4} to 10^{-3}nm/ps^2 [79,80]. In our study, the range of our acceleration is from 0.0005 to 0.002 nm/ps^2.

It should be noted that the fluid temperature in MD simulations is normally calculated from the kinetic energy via summation of the velocity-squared of all particles in the system[81]. However, the particle velocities along the direction of driving force are made up of two components: thermal velocity and center-of-mass velocity (the imposed streaming velocity). To ensure that the center-of-mass velocity does not contribute to the fluid temperature, only the velocity components perpendicular to the driving force are used to calculate the fluid temperature [76]. The temperature and pressure as a function of simulation time during NEMD simulations are presented in Fig. S2 in the Supporting Information.

3. Distribution of Water and Hydrocarbon in P-H and H-H Nanopores

Fig. 4 shows the equilibrium configurations and number density profiles (along z-direction) for water and hydrocarbon in 5 nm H-H (Fig.4a-b) and P-H (Fig. 4c-d) nanopores. We do not show the illite structure for clarity.

Fig. 4a shows a water film adjacent to the clay surfaces in the H-H pore system. Water preferentially adsorbs because of the strong electrostatic interaction between water and the surfaces[82] and the formation of a hydrogen bond between water and the surface hydroxyl and oxygen groups[83]. This observation is analogous to water adsorption in silica-based pore structures[76,84]. Increasing the water concentration to 58.82% as shown in Fig.4b leads to an increase in the adsorbed film thickness. The number density of water (shown in the blue line) and hydrocarbon (black solid line) are relatively constant across the pore.

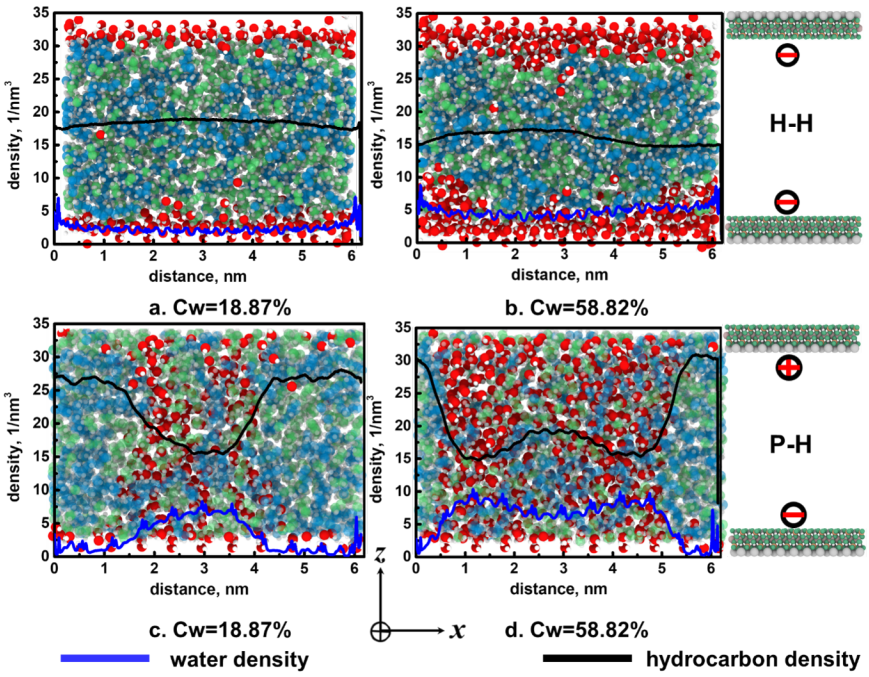

Fig. 4 Configurations and number density profiles of water (in blue) and hydrocarbon (in black) in hydroxyl-hydroxyl (H-H) and potassium-hydroxyl (P-H) pores with a width of 5 nm. Illite is not shown for clarity. The results show that P-H surfaces favor the formation of a water bridge, while adsorption is dominant in H-H pore systems.

The distribution of water in P-H pores is in marked contrast to the H-H nanopores. Fig. 4c shows the formation of a water bridge (corresponding to the peak in the number density of water shown in a blue line) at a water concentration of 18.87%. Increasing the water concentration to 58.82% as shown in Fig.4d leads to the formation of two water bridges indicated by the presence of two peaks in the water density profile. This phenomenon is commonly referred to as 'capillary condensation'[84–86]. However, the water bridge in the P-H nanopore persists even after increasing the pore size to 10 nm and 15 nm as shown in Fig.S-3 in Supporting Information. The water bridges observed in this work are not solely due to 'capillary condensation' which usually occurs when two water films are adequately close to each other[87]. Our work in this section tries to shed light on the existence of water bridges in P-H nanopores.

It is important to note that under certain conditions, a water bridge can form in an H-H clay-hosted pore, typically at higher water concentrations and for smaller pore widths. Table 1 shows the conditions under which a water bridge occurs.

Table 1 . The matrix below shows the conditions investigated in this study under which a water bridge will form.

		H-H			P-H		
		5nm	10nm	15nm	5nm	10nm	15nm
Water concentration	0	NA	NA	NA	NA	NA	NA
	18%				X	X	X
	56%				X	X	X
	71%	X	X		X	X	X
	80%	X	X	X	X	X	X
	100%	NA	NA	NA	NA	NA	NA

3.1 Analysis of the Electric Field

Inspired by the work of Zhang et al.[88], Namin et al.[89], Fuchs et al. [90,91], Ponterio et al. [92], and Chen et al. [93] who indicate that an electric field can change the OH stretching band and water distribution, our hypothesis is that the positively nonbonded cations (potassium layer) and negatively charged surface (hydroxyl layer) in clay nanopores might induce an electric field. This in turn dictates the behavior of confined fluids of water and hydrocarbons leading to the formation of water bridges. In order to validate this hypothesis, we calculate the electric field by numerically measuring the electrostatic force on a test atom with charge e .

This is done by probing a cross-section of the pores devoid of any fluid. Fig.5 shows the calculated electric field in 5 nm, 10 nm and 15 nm P-H and H-H pores. The average strengths of electric field in 5 nm, 10 nm and 15 nm P-H pores, as shown in Fig.5a, are 12.92 V/nm, 8.72 V/nm, 6.56 V/nm with standard deviation of 0.51, 0.39 and 0.44 respectively. While in theory the electric field should be uniform[94], non-uniformly distributed charges in the clay minerals cause variations in the electric field near the clay surface.

Fig. 5b shows the calculated electric field in 5 nm, 10 nm and 15 nm H-H pores which range from -1.5 V/nm and 1.5 V/nm. In Fig.5b, near the upper surface, the strength of electric field is about 1.5 V/nm. Moving across the pore, the field strength decreases to zero and its absolute value increases again (with an accompanying change in direction). Such electric fields have also been observed to occur naturally in zeolite cavities[95–97]. In both pore systems, an increase in pore width is accompanied by a decrease in electric field strength, an observation that is consistent with Bueno et al.[94].

Skinner et al.[98], Cramer et al.[99]and Hao et al.[32] also indicate that electric field strengths larger than 1 V/nm cause significant directional-dependence in the structure of water. A comparison of the electric fields in Figs.5a-b suggests that P-H pores exhibit stronger and more long-range fields in comparison to H-H pores. In the H-H pore, the effective length of the electric field > 1V/nm is about 0.5 nm as shown in Fig.5b impacting the water distribution only near the surface. In the P-H nanopore, a strong electric field extends across the entire pore width promoting the formation of water bridges.

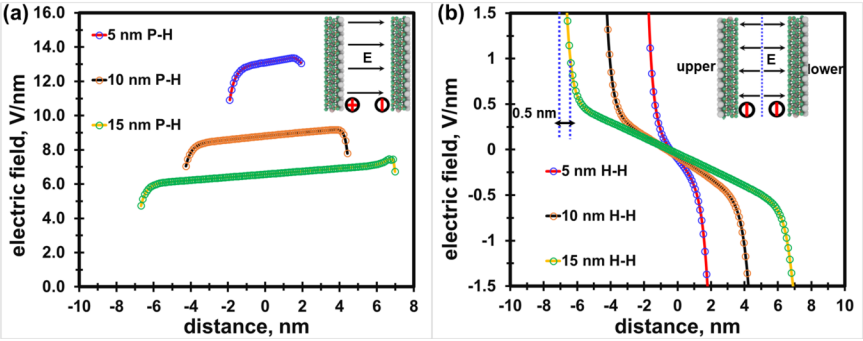

Fig. 5 Calculated electric field in P-H and H-H pores of different width. Absolute values of the electric field strengths in P-H pores are observed to be larger than those in H-H nanopores. Increases in pore width decreases the strength of the electric field in both P-H and H-H pores.

In Fig.6, we discuss the orientation of the water molecules at a concentration of 58.82% in both P-H and H-H pores. The orientational angle ϑ is defined as the angle between the OH vector and the unit vector normal to the surface in the z-direction (Fig. 6a). Fig. 6b shows one sharp peak in the P-H pore at 130° indicating that the two OH bonds are aligned with the direction of the electric field. These results are similar to those presented in Skinner et al.[98]. The OH bond orientation in H-H pores is more heterogeneous with a relatively weaker peak at 90°, which is consistent with Cramer et al. [99]. Figs. 5 and 6 confirm that the presence of electric field influences the orientation of water molecules within the pore.

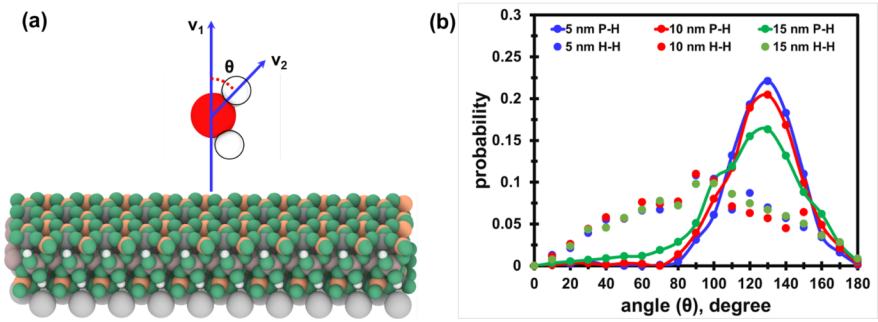

Fig. 6 In (a), V1 is the unit vector normal to the surface. V2 is the vector pointing from O to the H atom (OH bond angle). ϑ is the angle between the two vectors. In (b), we show the OH bond angle for all water molecules for different pore widths in H-H and P-H pores. In P-H pores, a dominant angle of 130° is observed while in H-H pores, the OH bond angles are largely random with a weaker peak at 90°. The electric field of **Fig. 5** influences the orientation of water molecules in both pore systems.

4 Results and Discussion: Fluid Transport

4.1 Fluid Transport in H-H Nanopores

In this section, we report on the hydrocarbon and water velocity profiles driven by different accelerations (0.0005, 0.001, and 0.002 nm/ps^2) at 350 K and 400 atm. This would be analogous to imposing advective flow on the fluid confined within the pores. The velocity profile is calculated using the bin method[100], and the details are provided in the Supporting Information.

We present the water (Fig. 7a) and hydrocarbon (Fig. 7b) velocity profiles at an acceleration of 0.0005 nm/ps^2 in the 5 nm H-H nanopore. Because the hydrocarbon and water velocity profiles at the acceleration of 0.001 nm/ps^2 and 0.002 nm/ps^2 show similar trends with that of 0.0005 nm/ps^2, they are not shown here and provided in Fig.S4 in Supporting Information.

Fig. 7a indicates that the water velocity changes with increasing water concentration directly as a result of the growth in the thickness of the adsorbed layer of water as shown in Fig. 8. A thicker adsorbed layer impedes flow. At 100% water, we observe the classical parabolic signature of liquid flow in slit-pores.

Fig. 7b indicates that increasing water concentration promotes hydrocarbon flow up to a point. The initial increase has been attributed to the creation of smooth surfaces following adsorption of water[76]. Subsequent increases decrease the effective flow radius for hydrocarbon flow as shown in Fig. 8, leading to a decline of hydrocarbon velocity.

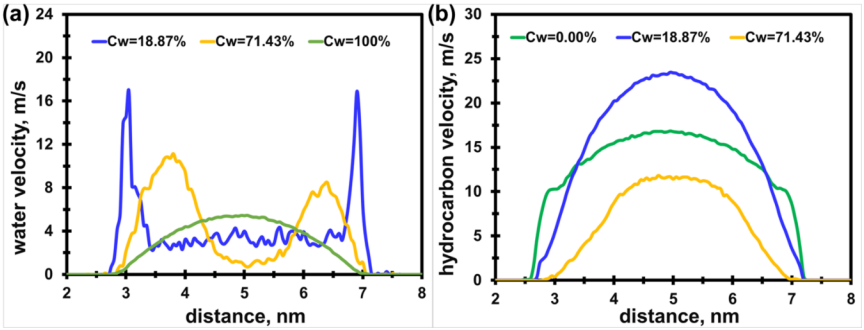

Fig.7 Water and hydrocarbon velocity profiles at an acceleration of 0.0005 nm/ps^2 in 5 nm H-H nanopore. Cw stands for water concentration. Water concentration is seen to strongly impact both water and hydrocarbon velocities.

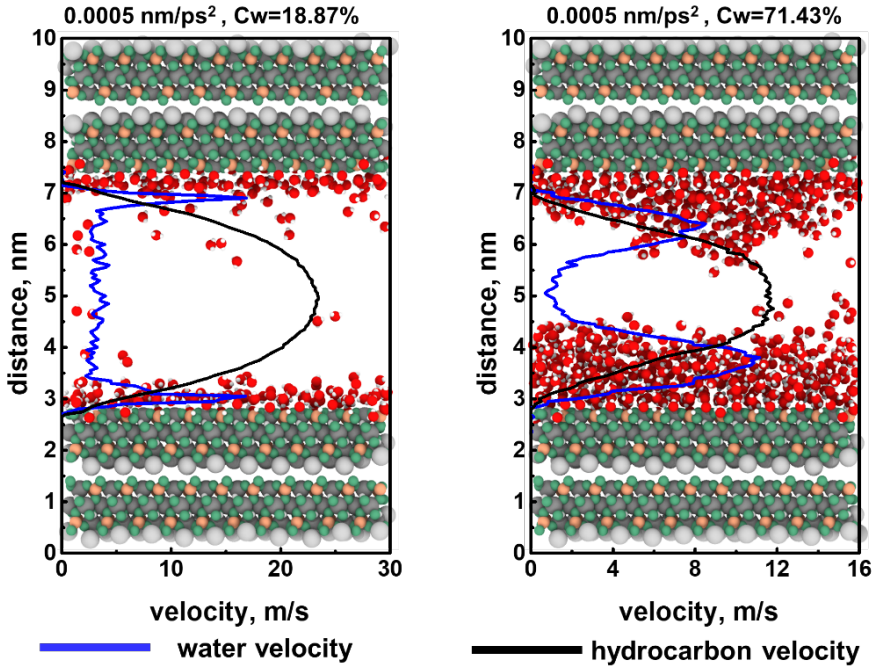

Fig. 8 Distribution of water molecules for various water concentrations. Hydrocarbon is not shown. On the left, Cw = 18.97% and on the right, Cw = 71.43%. Increases in water concentration increases the adsorbed layer thickness that in turn influences water and hydrocarbon velocities.

Fig. 9 shows the water and hydrocarbon velocity profiles at a higher value of acceleration of 0.002 nm/ps^2 in a larger 15 nm H-H nanopore (velocity profiles for the 10 nm H-H nanopore are provided in Fig. S5 in Supporting Information). The flow profiles are observed to be more complex at all values of saturation and is a function of the location of the respective phases within the pore.

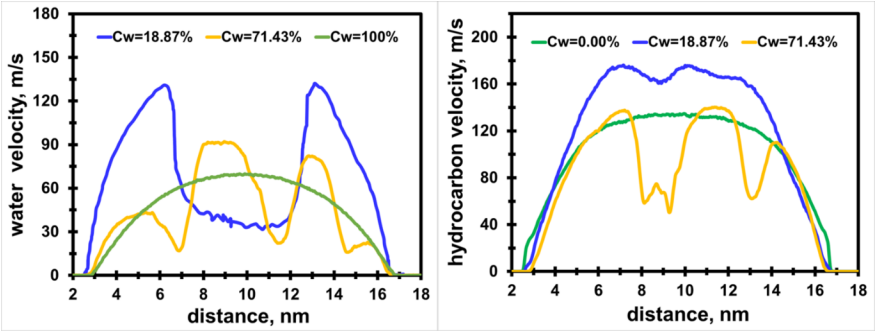

Fig. 9 Water and hydrocarbon velocity profiles at an acceleration of 0.002 nm/ps^2 in 15 nm H-H pores. The flow profiles for both phases appear more complex and simply correspond to the local phase densities within the pore.

Fig.10 shows the velocity profiles in a 5 nm, 10nm and 15nm H-H pore with a water concentration of 71.43%. The peaks and the troughs in the velocity profiles correspond to the local density of the water and hydrocarbon phases within the pore.

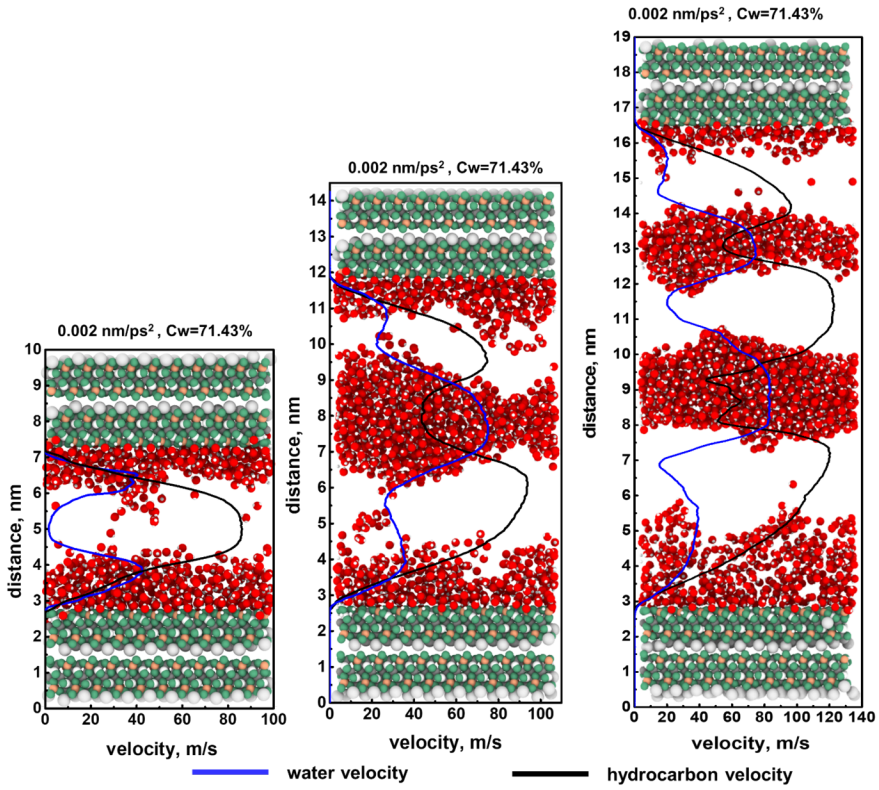

Fig. 10 Distribution of water at an acceleration of 0.002 nm/ps^2 and Cw = 71.43% in 5nm, 10nm, 15nm H-H pores. The hydrocarbon molecules are not shown. The result indicates that at each pore size, the peaks and troughs in the velocity profiles correspond to the local density of each of the phases.

4.2 Fluid Transport in P-H Nanopores

In the previous section, we reviewed transport of water and hydrocarbon in H-H pore systems where water bridges are largely absent except under some specific conditions. In this section, we present the corresponding results for P-H pores where water bridges are prevalent across multiple pore sizes and water concentrations.

The water and hydrocarbon velocity profiles for 54 NEMD simulations in P-H nanopore are provided in Figs. S6-7 in Supporting Information. In this section, we only analyze a few representative hydrocarbon-water velocity profiles in P-H nanopores and address the effects of pore size, water concentration and electric field (the effects of acceleration are provided in Supporting Information).

Effect of Pore size

Fig.11 shows the water (Fig.11a) and hydrocarbon (Fig.11b) velocity profiles at an acceleration and water concentration of 0.002 nm/ps^2 and 71.43% respectively in different P-H nanopore sizes. Water and hydrocarbon velocities increase with an increase of pore size which is in agreement with Liu et al.[41]. Additionally, water and hydrocarbon velocity profiles are parabolic in the 5 nm P-H nanopore and show flatter profiles for the 10nm and 15nm pores with increasing distance from the pore walls and the accompanying decrease in fluid-pore wall interactions.

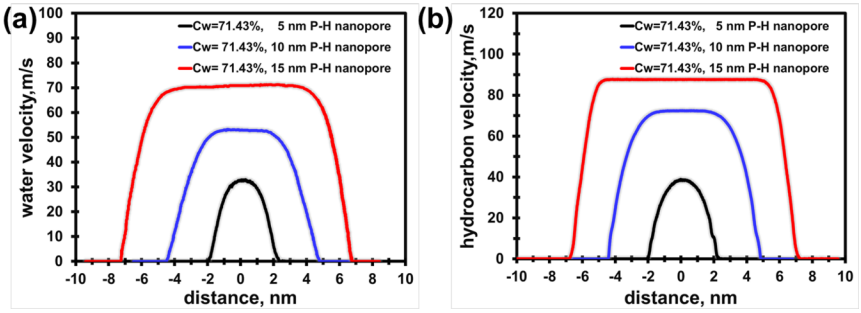

Fig. 11 Water and hydrocarbon velocity profiles at the acceleration and water concentration of 0.002 nm/ps^{2}and 71.43% respectively in different P-H nanopore sizes. The result indicates that pore size impacts the velocity patterns. At 5nm, we observe a parabolic shape for the flow profiles which get progressively flatter as the pore size increases.

In Fig. 12, we take a closer look at the water bridges present in the P-H pores at a water concentration of 71.43%. Hydrocarbon molecules are not shown for clarity. The red-colored water molecules are those adjacent to the pore surface and the yellow-colored water molecules are those present in the water bridge. Fig. 12a shows the distribution of water in a 5nm P-H pore obtained from our equilibrium MD (EMD simulations) on top and under an acceleration of 0.002 nm/ps^2 on the bottom. It should be noted that the water bridge in Fig. 12a is a sheet extending across the entire x-direction in the 5nm P-H nanopore.

Figs. 12b-c show the corresponding information for 10nm and 15nm pore widths respectively. Water molecules move freely between the water bridge and adsorbed layer resulting in the velocity profile in Fig. 12a (shown in a blue line). However, when pore sizes increase to 10 nm or 15 nm, there is limited or no exchange of water molecules between the film and the bridge. The combination of a constant acceleration and no exchange contributes to the flat velocity profiles observed in Figs. 12b-c.

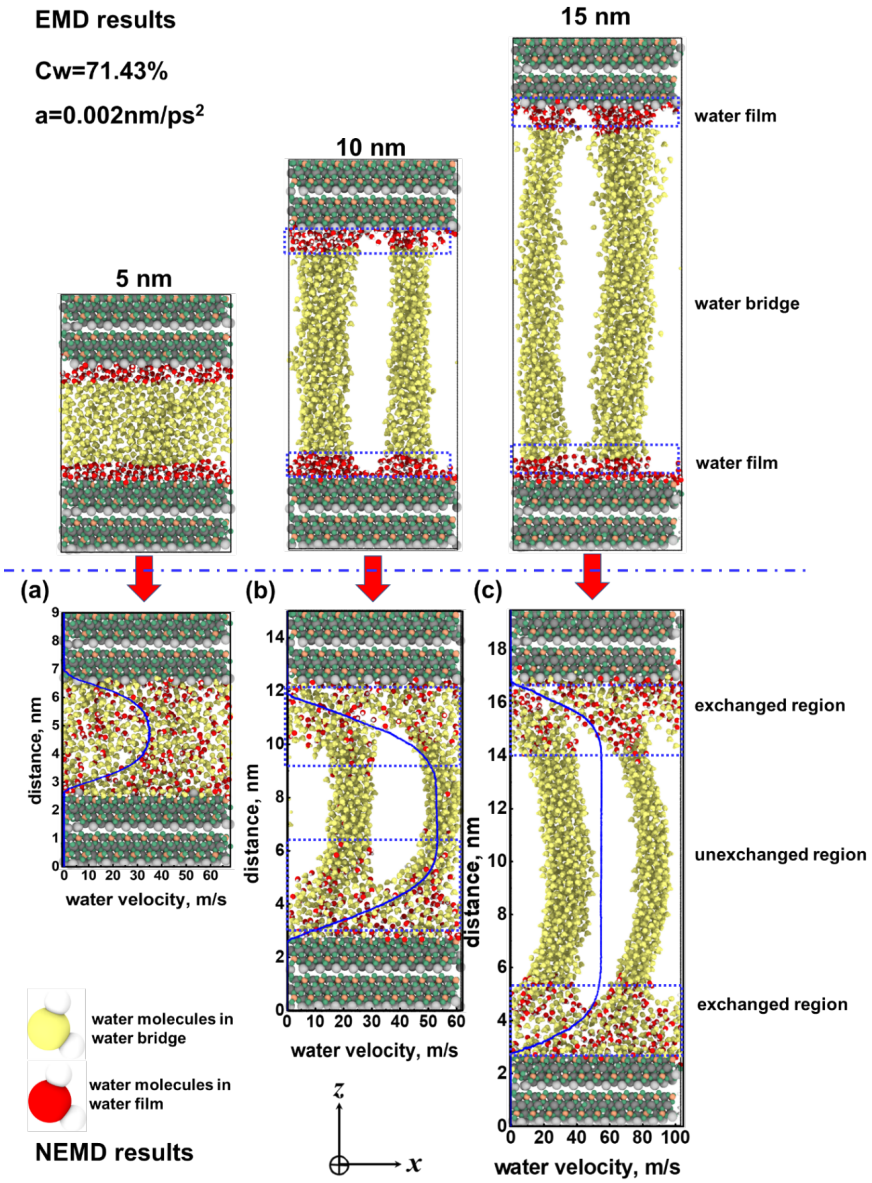

Fig. 12 Molecular distribution and velocity profiles of water in P-H pores of different widths at a water concentration of 71.43%. The acceleration is 0.002 nm/ps^2. Hydrocarbon is not shown for clarity. The red dots represent adsorbed water and the yellow dots are those in the water bridge. In a 5 nm P-H nanopore, acceleration causes the adsorbed layer to exchange both mass and velocity with water at the pore center. When the pore size increases to 10 nm or 15 nm, as revealed by the flatter velocity profile, no mass or velocity exchange occurs between the adsorbed layer and water in the bridge or pore center.

Effect of Water Concentration

Fig.13 shows the water (Fig.13a) and hydrocarbon (Fig.13b) velocity profiles at an acceleration of 0.002 nm/ps^2 in a 10 nm P-H nanopore for different values of water concentration. The velocity of water decreases with increasing water concentration (Fig. 13a) because of the increased thickness of the water bridge. The minimum thickness of the water bridge at concentrations of 18.87%, 58.82%, 71.43% and 80.00% is 0.94 nm,

1.24 nm, 1.60 nm and 1.96 nm respectively. This is shown in Fig. S9 in Supporting Information.

Fig. 13b shows an increased hydrocarbon velocity for an initial increase in the water concentration which has been attributed to the creation of smoother surfaces for hydrocarbon flow[76]. However, as the water concentration increases, the width of the water bridge progressively increases (shown in Fig S9), thereby hampering hydrocarbon flow.

Fig. 13 also indicates flat velocity profiles exist for both the oil and water phases. Because of the hydrophilic surface, hydrocarbon molecules are responding to the acceleration and are not strongly influenced by the pore surfaces, leading to a flatter velocity profile.

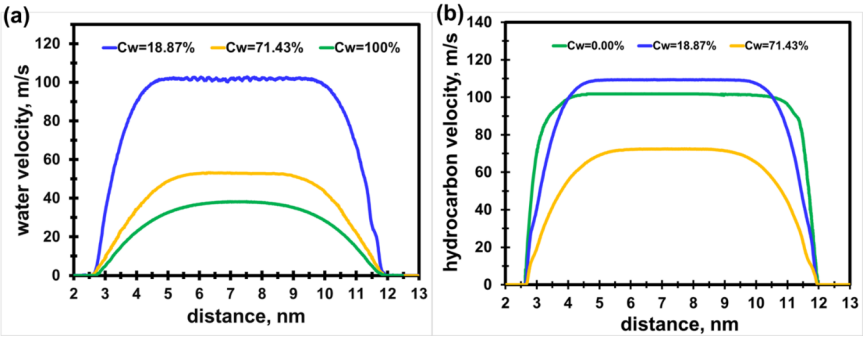

Fig. 13 Water and hydrocarbon velocity profiles at the acceleration of 0.002 nm/ps^2 in 10 nm P-H nanopore. The result indicates that water concentration can impact the flow pattern.

5. Single-Phase Velocity Profile Comparison between H-H and P-H Pores

This section focuses on the effect of the electric field single-phase velocities for different pore sizes for a fixed acceleration of 0.002 nm/ps^2 in P-H and H-H pores. The results are shown in Fig. 14 indicating that the P-H nanopore exhibits flatter flow profiles at the pore center due to the presence of the electric field as shown in Fig.5.

Normally, adsorption is the result of van der Waals forces, covalent bonding and electrostatic attraction[101]. In this work, we do not consider covalent bonding[102]. Therefore, in our study, adsorption is solely due to the van der Waals force and electrostatic attraction. Adjacent to the surface, these forces impact fluid transport. However, van der Waals force quickly diminish for increasing distances from the pore surface [103], while the long-range electrostatic interaction can extend tens of nanometers[32].

Therefore, in the P-H pore, fluid transport is controlled by the electric field and imposed acceleration, leading to a flat pattern as shown in Figs.14a-b. Increasing pore sizes for P-H pores increases the width of flat pattern as shown in Figs.14c-d because of the increase in the width of the zone dominated by the electric field. However, in H-H nanopore, there is a negligible electric field at the nanopore center. Therefore, classical parabolic shaped patterns are observed in H-H nanopores as shown in Fig.14.

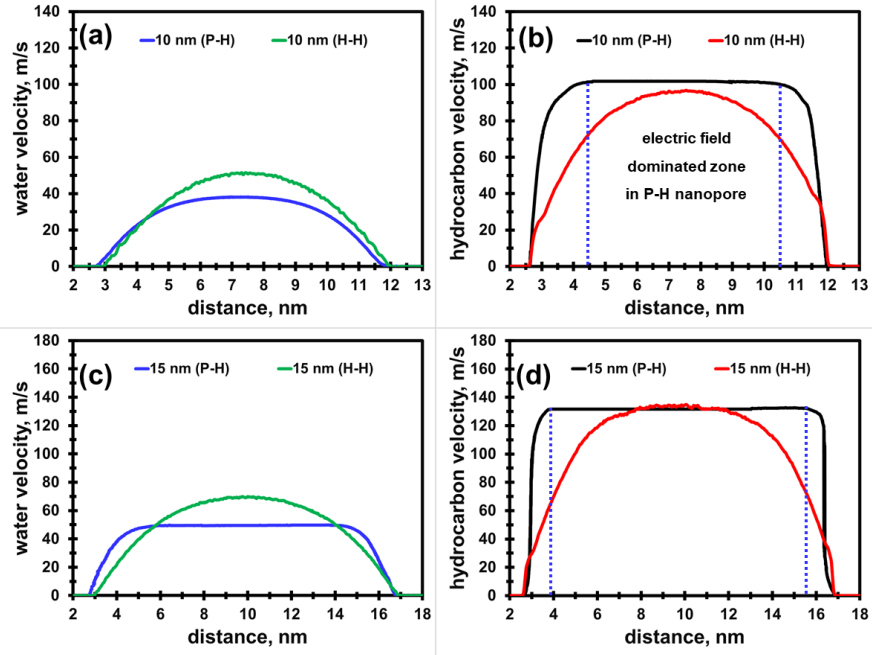

Fig. 14 Comparison of single phase (water and hydrocarbon) velocities between H-H and P-H nanopores of different widths. The self-generated electric field in P-H pores and the imposed acceleration dictate fluid transport in the center of the pore. For the same acceleration, the fluid velocity profile is flat in P-H pores and parabolic in H-H pores.

Fig. 15 shows the distribution of water in 5 nm P-H and H-H nanopores. Hydrocarbon is not shown for clarity. During transport, a water bridge persists in P-H pores as shown in Fig.15a. This is because of the stronger electric field. Fig.12 also confirm the persistence of water bridges in P-H pores irrespective of pore size. However, the water bridge of the H-H nanopore breaks down as shown in Fig.15b. We can infer that the strength of the hydrogen bond in the water bridge in the H-H nanopore is weaker compared to the forces holding the water bridge intact in the P-H nanopores.

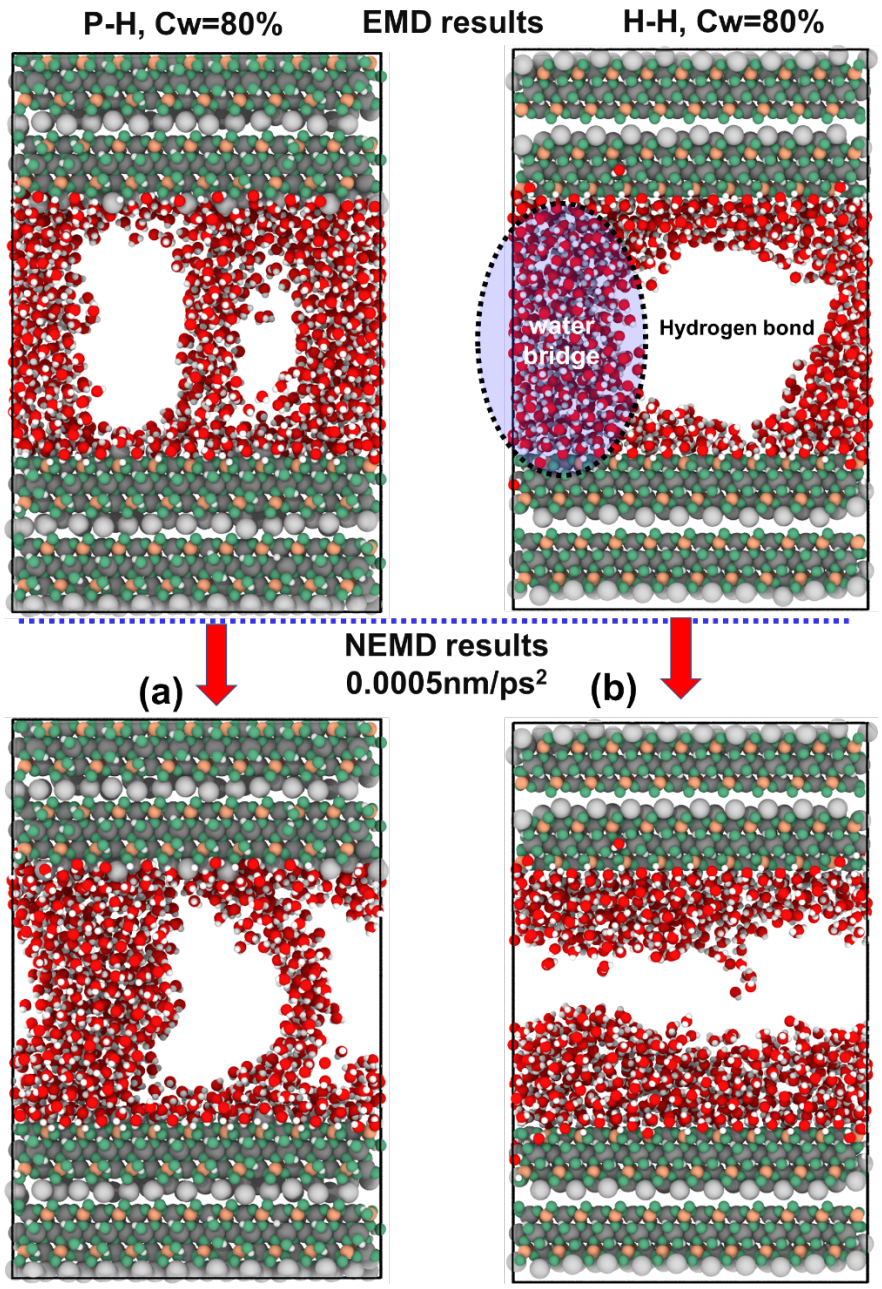

Fig. 15 Water distribution in EMD and NEMD simulations in 5 nm P-H (left) and H-H (right) nanopore. Hydrocarbons are not shown for clarity. The results indicate that the water bridge breaks down during flow in the NEMD simulation in the H-H nanopore, demonstrating that the strength of hydrogen bond is not strong enough to support the water bridge. However, in P-H nanopore, with the assistance of electric field, the water bridge persists in NEMD simulations.

5. Conclusions

This study focuses on the use of Equilibrium Molecular Dynamics (EMD) and Non-equilibrium MD (NEMD) simulations to investigate hydrocarbon-water interactions, structure and transport in clay-hosted nanopores with two different charged clay surface chemistries (H-H and P-H nanopores). The following conclusions can be drawn from this work:

1. Under a wide range of water concentration and pore sizes, P-H clay pores support the formation of water bridges. In H-H pores, water is largely present adjacent to the pore surface in an adsorbed layer. There are limited instances where a water bridge forms in an H-H pore, however.
2. The strength of the self-generated electric field is stronger in P-H pores in comparison to H-H pores for all pore widths. This promotes the formation of a water bridge and strong alignment of the water molecules with the electric field.
3. With an imposed acceleration, the velocity profiles in H-H and P-H clay pores are different. Water preferentially flows adjacent to the pore surface for H-H pores with hydrocarbon occupying the center of the pore. With P-H pores, the water bridge persists under acceleration and a different velocity profile is observed irrespective of pore width.
4. As mentioned earlier, in H-H pores, water bridges can form under specific conditions, but dissipate during flow. However, in P-H nanopores, with the assistance of the electric field, water bridges exist under flowing conditions.

Acknowledgements

The computing for this project was performed at the OU Supercomputing Center for Education & Research (OSCER) at the University of Oklahoma. We thank Drs. Carl Sondergeld, Chandra Rai, Ali Tinni and Felipe Perez for feedback that helped shape this work.

References

(1) Sparreboom, W.; Van Den Berg, A.; Eijkel, J. C. T. Principles and Applications of Nanofluidic Transport. *Nat. Nanotechnol.***2009** , *4* (11), 713–720. https://doi.org/10.1038/nnano.2009.332.

(2) Ball, P. Water as an Active Constituent in Cell Biology. *Chem. Rev.* **2008** , *108* (1), 74–108. https://doi.org/10.1021/cr068037a.

(3) Joshi, R. K.; Carbone, P.; Wang, F. C.; Kravets, V. G.; Su, Y.; Grigorieva, I. V.; Wu, H. A.; Geim, A. K.; Nair, R. R. Precise and Ultrafast Molecular Sieving through Graphene Oxide Membranes.*Science (80-.).* **2014** , *343* (6172), 752–754. https://doi.org/10.1126/science.1245711.

(4) Heuberger, M.; Zäch, M.; Spencer, N. D. Density Fluctuations under Confinement: When Is a Fluid Not a Fluid? *Science (80-.).***2001** , *292* (5518), 905–908. https://doi.org/10.1126/science.1058573.

(5) Scatena, L. F.; Brown, M. G.; Richmond, G. L. Water at Hydrophobic Surfaces: Weak Hydrogen Bonding and Strong Orientation Effects.*Science (80-.).* **2001** , *292* (5518), 908–912. https://doi.org/10.1126/science.1059514.

(6) Werder, T.; Walther, J. H.; Jaffe, R. L.; Halicioglu, T.; Noca, F.; Koumoutsakos, P. Molecular Dynamics Simulation of Contact Angles of Water Droplets in Carbon Nanotubes. *Nano Lett.* **2001** ,*1* (12), 697–702. https://doi.org/10.1021/nl015640u.

(7) Levinger, N. E. Chemistry: Water in Confinement. *Science (80-.).* **2002** , *298* (5599), 1722–1723. https://doi.org/10.1126/science.1079322.

(8) Rivera, J. L.; McCabe, C.; Cummings, P. T. Layering Behavior and Axial Phase Equilibria of Pure Water and Water + Carbon Dioxide Inside Single Wall Carbon Nanotubes. *Nano Lett.* **2002** , *2*(12), 1427–1431. https://doi.org/10.1021/nl0257566.

(9) Kofinger, J.; Hummer, G.; Dellago, C. Macroscopically Ordered Water in Nanopores. *Proc. Natl. Acad. Sci.* **2008** , *105*(36), 13218–13222. https://doi.org/10.1073/pnas.0801448105.

(10) Ma, M.; Grey, F.; Shen, L.; Urbakh, M.; Wu, S.; Liu, J. Z.; Liu, Y.; Zheng, Q. Water Transport inside Carbon Nanotubes Mediated by Phonon-Induced Oscillating Friction. *Nat. Nanotechnol.***2015** , *10* (8), 692–695. https://doi.org/10.1038/nnano.2015.134.

(11) Wu, K.; Dong, X.; Li, X.; Li, J.; Xu, J.; Chen, Z. Wettability Effect on Nanoconfined Water Flow. *Proc. Natl. Acad. Sci.***2017** , *114* (13), 3358–3363. https://doi.org/10.1073/pnas.1612608114.

(12) Wu, K.; Chen, Z.; Li, J.; Lei, Z.; Xu, J.; Wang, K.; Li, R.; Dong, X.; Peng, Y.; Yang, S.; et al. Nanoconfinement Effect on N-Alkane Flow.*J. Phys. Chem. C* **2019** . https://doi.org/10.1021/acs.jpcc.9b03903.

(13) Brown, M. A.; Abbas, Z.; Kleibert, A.; Green, R. G.; Goel, A.; May, S.; Squires, T. M. Determination of Surface Potential and Electrical Double-Layer Structure at the Aqueous Electrolyte-Nanoparticle Interface. *Phys. Rev. X* **2016** , *6* (1), 1–12. https://doi.org/10.1103/PhysRevX.6.011007.

(14) Brown, M. A.; Goel, A.; Abbas, Z. Effect of Electrolyte Concentration on the Stern Layer Thickness at a Charged Interface.*Angew. Chemie - Int. Ed.* **2016** , *55* (11), 3790–3794. https://doi.org/10.1002/anie.201512025.

(15) Azam, M. S.; Weeraman, C. N.; Gibbs-Davis, J. M. Specific Cation Effects on the Bimodal Acid-Base Behavior of the Silica/Water Interface.*J. Phys. Chem. Lett.* **2012** , *3* (10), 1269–1274. https://doi.org/10.1021/jz300255x.

(16) Jena, K. C.; Covert, P. A.; Hore, D. K. The Effect of Salt on the Water Structure at a Charged Solid Surface: Differentiating Second- and Third-Order Nonlinear Contributions. *J. Phys. Chem. Lett.***2011** , *2* (9), 1056–1061. https://doi.org/10.1021/jz200251h.

(17) Urashima, S. H.; Myalitsin, A.; Nihonyanagi, S.; Tahara, T. The Topmost Water Structure at a Charged Silica/Aqueous Interface Revealed by Heterodyne-Detected Vibrational Sum Frequency Generation Spectroscopy. *J. Phys. Chem. Lett.* **2018** , *9* (14), 4109–4114. https://doi.org/10.1021/acs.jpclett.8b01650.

(18) Dobrynin, A. V.; Rubinstein, M.; Joanny, J. F. Adsorption of a Polyampholyte Chain on a Charged Surface. *Macromolecules***1997** , *30* (15), 4332–4341. https://doi.org/10.1021/ma9703057.

(19) Zhang, L.; Sun, Y. Charged Surface Regulates the Molecular Interactions of Electrostatically Repulsive Peptides by Inducing Oriented Alignment. *Langmuir* **2018** , *34* (14), 4390–4397. https://doi.org/10.1021/acs.langmuir.7b04308.

(20) Tasca, F.; Harreither, W.; Ludwig, R.; Gooding, J. J.; Gorton, L. Cellobiose Dehydrogenase Aryl Diazonium Modified Single Walled Carbon Nanotubes: Enhanced Direct Electron Transfer through a Positively Charged Surface. *Anal. Chem.* **2011** , *83* (8), 3042–3049. https://doi.org/10.1021/ac103250b.

(21) Dreier, L. B.; Nagata, Y.; Lutz, H.; Gonella, G.; Hunger, J.; Backus, E. H. G.; Bonn, M. Saturation of Charge-Induced Water Alignment at Model Membrane Surfaces. *Sci. Adv.* **2018** , *4*(3), 1–9. https://doi.org/10.1126/sciadv.aap7415.

(22) David Ehre, Etay Lavert, Meir Lahav, I. L. Water Freezes Differently on Positively and Negatively Charged Surfaces of Pyroelectric Materials. *Science (80-.).* **2010** , No. February, 672–675.

(23) Lahann, J.; Mitragotri, S.; Tran, T. N.; Kaido, H.; Sundaram, J.; Choi, I. S.; Hoffer, S.; Somorjai, G. A.; Langer, R. A Reversibly Switching Surface. *Science (80-.).* **2003** , *299*(5605), 371–374. https://doi.org/10.1126/science.1078933.

(24) Lis, D.; Backus, E. H. G.; Hunger, J.; Parekh, S. H.; Bonn, M. Liquid Flow along a Solid Surface Reversibly Alters Interfacial Chemistry. *Science (80-.).* **2014** , *344* (6188), 1138–1142. https://doi.org/10.1126/science.1253793.

(25) Jiménez-González, I.; Rodríguez-Navarro, C.; Scherer, G. W. Role of Clay Minerals in the Physicomechanical Deterioration of Sandstone.*J. Geophys. Res. Earth Surf.* **2008** , *113* (2), 1–17. https://doi.org/10.1029/2007JF000845.

(26) Uddin, M. K. A Review on the Adsorption of Heavy Metals by Clay Minerals, with Special Focus on the Past Decade. *Chem. Eng. J.***2017** , *308* (October), 438–462. https://doi.org/10.1016/j.cej.2016.09.029.

(27) Jeon, P. R.; Choi, J.; Yun, T. S.; Lee, C.-H. Sorption Equilibrium and Kinetics of CO2 on Clay Minerals from Subcritical to Supercritical Conditions: CO2 Sequestration at Nanoscale Interfaces. *Chem. Eng. J.* **2014** , *255* , 705–715. https://doi.org/10.1016/J.CEJ.2014.06.090.

(28) Cygan, R. T.; Romanov, V. N.; Myshakin, E. M. Molecular Simulation of Carbon Dioxide Capture by Montmorillonite Using an Accurate and Flexible Force Field. *J. Phys. Chem. C* **2012** , *116*(24), 13079–13091. https://doi.org/10.1021/jp3007574.

(29) Shannon, M. A.; Bohn, P. W.; Elimelech, M.; Georgiadis, J. G.; Marin, B. J.; Mayes, A. M. Shannon-M.A._Science-and-Technology-for-Water-Purification-in-the-Coming-Decades_2008.Pdf.**2008** , *452* (March), 301–310. https://doi.org/10.1038/nature06599.

(30) Hensen, E. J. M.; Smit, B. Why Clays Swell. *J. Phys. Chem. B***2002** , *106* (49), 12664–12667. https://doi.org/10.1021/jp0264883.

(31) Kuila, U.; Prasad, M. Specific Surface Area and Pore-Size Distribution in Clays and Shales. *Geophys. Prospect.***2013** , *61* (2), 341–362. https://doi.org/10.1111/1365-2478.12028.

(32) Hao, Y.; Jia, X.; Lu, Z.; Lu, D.; Li, P. Water Film or Water Bridge ? In Fl Uence of Self-Generated Electric Field on Coexisting Patterns of Water and Methane in Clay Nanopores. *J. Phys. Chem. C***2019** . https://doi.org/10.1021/acs.jpcc.9b06519.

(33) Chai, L.; Klein, J. Role of Ion Ligands in the Attachment of Poly(Ethylene Oxide) to a Charged Surface. *J. Am. Chem. Soc.***2005** , *127* (4), 1104–1105. https://doi.org/10.1021/ja043963x.

(34) Rigo, E.; Dong, Z.; Park, J. H.; Kennedy, E.; Hokmabadi, M.; Almonte-Garcia, L.; Ding, L.; Aluru, N.; Timp, G. Measurements of the Size and Correlations between Ions Using an Electrolytic Point Contact.*Nat. Commun.* **2019** , *10* (1), 2382. https://doi.org/10.1038/s41467-019-10265-2.

(35) Loganathan, N.; Kalinichev, A. G. Quantifying the Mechanisms of Site-Specific Ion Exchange at an Inhomogeneously Charged Surface: Case of Cs+/K+ on Hydrated Muscovite Mica. *J. Phys. Chem. C***2017** , *121* (14), 7829–7836. https://doi.org/10.1021/acs.jpcc.6b13108.

(36) Jungwirth, P.; Laage, D. Ion-Induced Long-Range Orientational Correlations in Water: Strong or Weak, Physiologically Relevant or Unimportant, and Unique to Water or Not? *J. Phys. Chem. Lett.***2018** , *9* (8), 2056–2057. https://doi.org/10.1021/acs.jpclett.8b01027.

(37) Dewhirst, M. W.; Secomb, T. W. Transport of Drugs from Blood Vessels to Tumour Tissue. *Nat. Rev. Cancer* **2017** ,*17* (12), 738–750. https://doi.org/10.1038/nrc.2017.93.

(38) Rao, S.; Chen, R.; LaRocca, A. A.; Christiansen, M. G.; Senko, A. W.; Shi, C. H.; Chiang, P.-H.; Varnavides, G.; Xue, J.; Zhou, Y.; et al. Remotely Controlled Chemomagnetic Modulation of Targeted Neural Circuits. *Nat. Nanotechnol.* **2019** , *14* (10), 967–973. https://doi.org/10.1038/s41565-019-0521-z.

(39) Warner, N. R.; Jackson, R. B.; Darrah, T. H.; Osborn, S. G.; Down, A.; Zhao, K.; White, A.; Vengosh, A. Geochemical Evidence for Possible Natural Migration of Marcellus Formation Brine to Shallow Aquifers in Pennsylvania. *Proc. Natl. Acad. Sci. U. S. A.* **2012** ,*109* (30), 11961–11966. https://doi.org/10.1073/pnas.1121181109.

(40) Cui, S. T.; McCabe, C.; Cummings, P. T.; Cochran, H. D. Molecular Dynamics Study of the Nano-Rheology of n-Dodecane Confined between Planar Surfaces. *J. Chem. Phys.* **2003** , *118* (19), 8941–8944. https://doi.org/10.1063/1.1568084.

(41) Liu, B.; Wang, C.; Zhang, J.; Xiao, S.; Zhang, Z.; Shen, Y.; Sun, B.; He, J. Displacement Mechanism of Oil in Shale Inorganic Nanopores by Supercritical Carbon Dioxide from Molecular Dynamics Simulations.*Energy and Fuels* **2017** , *31* (1), 738–746. https://doi.org/10.1021/acs.energyfuels.6b02377.

(42) Xiong, H.; Devegowda, D.; Huang, L. EOR Solvent-Oil Interaction in Clay-Hosted Pores: Insights from Molecular Dynamics Simulations.*Fuel* **2019** , *249* , 233–251. https://doi.org/10.1016/j.fuel.2019.03.104.

(43) Gualtieri, A. F.; Ferrari, S.; Leoni, M.; Grathoff, G.; Hugo, R.; Shatnawi, M.; Paglia, G.; Billinge, S. Structural Characterization of the Clay Mineral Illite-1M. *J. Appl. Crystallogr.* **2008** ,*41* (2), 402–415. https://doi.org/10.1107/S0021889808004202.

(44) Galan, E.; Ferrell, R. E. Genesis of Clay Minerals. *Dev. Clay Sci.* **2013** , *5* , 83–126. https://doi.org/10.1016/B978-0-08-098258-8.00003-1.

(45) Liu, J.; Li, P.; Sun, Z.; Lu, Z.; Du, Z.; Liang, H.; Lu, D. A New Method for Analysis of Dual Pore Size Distributions in Shale Using Nitrogen Adsorption Measurements. *Fuel* **2017** , *210*(August), 446–454. https://doi.org/10.1016/j.fuel.2017.08.067.

(46) Wang, Y.; Zhu, Y.; Chen, S.; Li, W. Characteristics of the Nanoscale Pore Structure in Northwestern Hunan Shale Gas Reservoirs Using Field Emission Scanning Electron Microscopy, High-Pressure Mercury Intrusion, and Gas Adsorption. *Energy and Fuels* **2014** ,*28* (2), 945–955. https://doi.org/10.1021/ef402159e.

(47) Li, J.; Li, X.; Wang, X.; Li, Y.; Wu, K.; Shi, J.; Yang, L.; Feng, D.; Zhang, T.; Yu, P. Water Distribution Characteristic and Effect on Methane Adsorption Capacity in Shale Clay. *Int. J. Coal Geol.***2016** , *159* , 135–154. https://doi.org/10.1016/j.coal.2016.03.012.

(48) Zhang, J.; Clennell, M. B.; Liu, K.; Pervukhina, M.; Chen, G.; Dewhurst, D. N. Methane and Carbon Dioxide Adsorption on Illite.*Energy and Fuels* **2016** , *30* (12), 10643–10652. https://doi.org/10.1021/acs.energyfuels.6b01776.

(49) Loewenstein, W. The Distribution of Aluminum in the Tetrahedra of Silicates and Aluminates. *Am. Mineral.* **1954** , *39* , 92–96. https://doi.org/10.1002/anie.201004007.

(50) Hao, Y.; Yuan, L.; Li, P.; Zhao, W.; Li, D.; Lu, D. Molecular Simulations of Methane Adsorption Behavior in Illite Nanopores Considering Basal and Edge Surfaces. *Energy and Fuels***2018** , *32* (4), 4783–4796. https://doi.org/10.1021/acs.energyfuels.8b00070.

(51) Jin, Z.; Firoozabadi, A. Methane and Carbon Dioxide Adsorption in Clay-like Slit Pores by Monte Carlo Simulations. *Fluid Phase Equilib.* **2013** , *360* , 456–465. https://doi.org/10.1016/j.fluid.2013.09.047.

(52) Jin, Z.; Firoozabadi, A. Effect of Water on Methane and Carbon Dioxide Sorption in Clay Minerals by Monte Carlo Simulations.*Fluid Phase Equilib.* **2014** , *382* , 10–20. https://doi.org/10.1016/j.fluid.2014.07.035.

(53) Cygan, R. T.; Liang, J.-J.; Kalinichev, A. G. Molecular Models of Hydroxide, Oxyhydroxide, and Clay Phases and the Development of a General Force Field. *J. Phys. Chem. B* **2004** , *108*(4), 1255–1266. https://doi.org/10.1021/jp0363287.

(54) Underwood, T.; Erastova, V.; Greenwell, H. C. Wetting Effects and Molecular Adsorption at Hydrated Kaolinite Clay Mineral Surfaces.*J. Phys. Chem. C* **2016** , *120* (21), 11433–11449. https://doi.org/10.1021/acs.jpcc.6b00187.

(55) Zen, A.; Roch, L. M.; Cox, S. J.; Hu, X. L.; Sorella, S.; Alfe, D.; Michaelides, A. Toward Accurate Adsorption Energetics on Clay Surfaces.*J. Phys. Chem. C* **2016** , *120* (46), 26402–26413. https://doi.org/10.1021/acs.jpcc.6b09559.

(56) Berendsen, H. J. C.; Postma, J. P. M.; van Gunsteren, W. F.; Hermans, J. Interaction Models for Water in Relation to Protein Hydration BT - Intermolecular Forces: Proceedings of the Fourteenth Jerusalem Symposium on Quantum Chemistry and Biochemistry Held in Jerusalem, Israel, April 13–16, 1981; Pullman, B., Ed.; Springer Netherlands: Dordrecht, 1981; pp 331–342. https://doi.org/10.1007/978-94-015-7658-1_21.

(57) Jorgensen, W. L.; Maxwell, D. S.; Tirado-Rives, J. Development and Testing of the OPLS All-Atom Force Field on Conformational Energetics and Properties of Organic Liquids. *J. Am. Chem. Soc.***1996** , *118* (45), 11225–11236. https://doi.org/10.1021/ja9621760.

(58) Wu, T.; Zhao, H.; Tesson, S.; Firoozabadi, A. Absolute Adsorption of Light Hydrocarbons and Carbon Dioxide in Shale Rock and Isolated Kerogen. *Fuel* **2019** , *235* , 855–867. https://doi.org/10.1016/J.FUEL.2018.08.023.

(59) Zhao, H.; Wu, T.; Firoozabadi, A. High Pressure Sorption of Various Hydrocarbons and Carbon Dioxide in Kimmeridge Blackstone and Isolated Kerogen. *Fuel* **2018** , *224* , 412–423. https://doi.org/10.1016/J.FUEL.2018.02.186.

(60) Plimpton, S. Fast Parallel Algorithms for Short-Range Molecular Dynamics. *J. Comput. Phys.* **1995** , *117* (1), 1–19. https://doi.org/https://doi.org/10.1006/jcph.1995.1039.

(61) Lennard-Jones, J. E. On the Determination o f Molecular Fields. — II. From the Equation o f State o f a Gas. *Proc. R. Soc. Lond.***1924** , *4* (71). https://doi.org/10.1098/rspa.1924.0082.

(62) Toukmaji, A. Y.; Board, J. A. Ewald Summation Techniques in Perspective: A Survey. *Comput. Phys. Commun.* **1996** ,*95* (2–3), 73–92. https://doi.org/10.1016/0010-4655(96)00016-1.

(63) Eastwood, J. W.; Hockney, R. W.; Lawrence, D. N. P3M3DP-the Three-Dimensional Periodic Particle-Particle/Particle-Mesh Program. *Comput. Phys. Commun.* **1984** , *35* , C–618. https://doi.org/10.1016/S0010-4655(84)82783-6.

(64) Martinez, J. M.; Martinez, L. Packing Optimization for Automated Generation of Complex System's Initial Configurations for Molecular Dynamics and Docking. *J. Comput. Chem.* **2003** , *24*(7), 819–825. https://doi.org/10.1002/jcc.10216.

(65) Parrinello, M.; Rahman, A. Polymorphic Transitions in Single Crystals: A New Molecular Dynamics Method. *J. Appl. Phys.***1981** , *52* (12), 7182–7190. https://doi.org/10.1063/1.328693.

(66) Nose, S. A Unified Formulation of the Constant Temperature Molecular Dynamics Methods. *J. Chem. Phys.* **1984** ,*81* (1), 511–519. https://doi.org/10.1063/1.447334.

(67) Malevanets, A.; Kapral, R. Solute Molecular Dynamics in a Mesoscale Solvent. *J. Chem. Phys.* **2000** , *112* (16), 7260–7269. https://doi.org/10.1063/1.481289.

(68) Malevanets, A. Mesoscopic Model for Solvent Dynamics. *J. Chem. Phys.* **1999** , *110* (17), 8605–8613. https://doi.org/10.1063/1.478857.

(69) Lamura, A.; Gompper, G.; Ihle, T.; Kroll, D. M. Multi-Particle Collision Dynamics : Flow around a Circular. *Europhys. Lett.***2001** , *56* (3), 319–325.

(70) Thomas, J. A.; McGaughey, A. J. H. Water Flow in Carbon Nanotubes: Transition to Subcontinuum Transport. *Phys. Rev. Lett.***2009** , *102* (18), 1–4. https://doi.org/10.1103/PhysRevLett.102.184502.

(71) Kalra, A.; Garde, S.; Hummer, G. Osmotic Water Transport through Carbon Nanotube Membranes. *Proc. Natl. Acad. Sci. U. S. A.***2003** , *100* (18), 10175–10180. https://doi.org/10.1073/pnas.1633354100.

(72) Nikoubashman, A.; Likos, C. N. Flow-Induced Polymer Translocation through Narrow and Patterned Channels. *J. Chem. Phys.***2010** , *133* (7). https://doi.org/10.1063/1.3466918.

(73) Nikoubashman, A.; Likos, C. N.; Kahl, G. Computer Simulations of Colloidal Particles under Flow in Microfluidic Channels. *Soft Matter* **2013** , *9* (9), 2603–2613. https://doi.org/10.1039/c2sm26727f.

(74) Allahyarov, E.; Gompper, G. Mesoscopic Solvent Simulations: Multiparticle-Collision Dynamics of Three-Dimensional Flows. *Phys. Rev. E - Stat. Physics, Plasmas, Fluids, Relat. Interdiscip. Top.***2002** , *66* (3), 1–9. https://doi.org/10.1103/PhysRevE.66.036702.

(75) Liu, B.; Wu, R.; Baimova, J. A.; Wu, H.; Law, A. W. K.; Dmitriev, S. V.; Zhou, K. Molecular Dynamics Study of Pressure-Driven Water Transport through Graphene Bilayers. *Phys. Chem. Chem. Phys.***2016** , *18* (3), 1886–1896. https://doi.org/10.1039/c5cp04976h.

(76) Liu, B.; Qi, C.; Zhao, X.; Teng, G.; Zhao, L.; Zheng, H.; Zhan, K.; Shi, J. Nanoscale Two-Phase Flow of Methane and Water in Shale Inorganic Matrix. *J. Phys. Chem. C* **2018** , *122* , 26671–26679. https://doi.org/10.1021/acs.jpcc.8b06780.

(77) Falk, K.; Sedlmeier, F.; Joly, L.; Netz, R. R.; Bocquet, L. Ultralow Liquid/Solid Friction in Carbon Nanotubes: Comprehensive Theory for Alcohols, Alkanes, OMCTS, and Water. *Langmuir* **2012** ,*28* (40), 14261–14272. https://doi.org/10.1021/la3029403.

(78) Wang, S.; Feng, Q.; Javadpour, F.; Yang, Y. B. Breakdown of Fast Mass Transport of Methane through Calcite Nanopores. *J. Phys. Chem. C* **2016** , *120* (26), 14260–14269. https://doi.org/10.1021/acs.jpcc.6b05511.

(79) Zhao, P.; Ma, H.; Rasouli, V.; Liu, W.; Cai, J.; Huang, Z. An Improved Model for Estimating the TOC in Shale Formations. *Mar. Pet. Geol.* **2017** , *83* , 174–183. https://doi.org/10.1016/J.MARPETGEO.2017.03.018.

(80) Wang, S.; Javadpour, F.; Feng, Q. Molecular Dynamics Simulations of Oil Transport through Inorganic Nanopores in Shale. *Fuel***2016** , *171* , 74–86. https://doi.org/10.1016/j.fuel.2015.12.071.

(81) Wang, S.; Javadpour, F.; Feng, Q. Fast Mass Transport of Oil and Supercritical Carbon Dioxide through Organic Nanopores in Shale.*Fuel* **2016** , *181* , 741–758. https://doi.org/10.1016/j.fuel.2016.05.057.

(82) Phan, A.; Ho, T. A.; Cole, D. R.; Striolo, A. Molecular Structure and Dynamics in Thin Water Films at Metal Oxide Surfaces: Magnesium, Aluminum, and Silicon Oxide Surfaces. *J. Phys. Chem. C***2012** , *116* (30), 15962–15973. https://doi.org/10.1021/jp300679v.

(83) Bourg, I. C.; Steefel, C. I. Molecular Dynamics Simulations of Water Structure and Diffusion in Silica Nanopores. *J. Phys. Chem. C* **2012** , *116* (21), 11556–11564. https://doi.org/10.1021/jp301299a.

(84) Yamashita, K.; Daiguji, H. Molecular Simulations of Water Adsorbed on Mesoporous Silica Thin Films. *J. Phys. Chem. C* **2013** ,*117* (5), 2084–2095. https://doi.org/10.1021/jp312804c.

(85) Tan, S. P.; Piri, M. Equation-of-State Modeling of Associating-Fluids Phase Equilibria in Nanopores. *Fluid Phase Equilib.* **2015** , *405* , 157–166. https://doi.org/10.1016/j.fluid.2015.07.044.

(86) Danov, K. D.; Georgiev, M. T.; Kralchevsky, P. A.; Radulova, G. M.; Gurkov, T. D.; Stoyanov, S. D.; Pelan, E. G. Hardening of Particle/Oil/Water Suspensions Due to Capillary Bridges: Experimental Yield Stress and Theoretical Interpretation. *Adv. Colloid Interface Sci.* **2018** , *251* (December), 80–96. https://doi.org/10.1016/j.cis.2017.11.004.

(87) Zhong, J.; Riordon, J.; Zandavi, S. H.; Xu, Y.; Persad, A. H.; Mostowfi, F.; Sinton, D. Capillary Condensation in 8 Nm Deep Channels.*J. Phys. Chem. Lett.* **2018** , *9* (3), 497–503. https://doi.org/10.1021/acs.jpclett.7b03003.

(88) Zhang, C.; Hutter, J.; Sprik, M. Coupling of Surface Chemistry and Electric Double Layer at TiO 2 Electrochemical Interfaces . *J. Phys. Chem. Lett.* **2019** , *10* (14), 3871–3876. https://doi.org/10.1021/acs.jpclett.9b01355.

(89) Montazeri Namin, R.; Azizpour Lindi, S.; Amjadi, A.; Jafari, N.; Irajizad, P. Experimental Investigation of the Stability of the Floating Water Bridge. *Phys. Rev. E - Stat. Nonlinear, Soft Matter Phys.***2013** , *88* (3), 1–6. https://doi.org/10.1103/PhysRevE.88.033019.

(90) Fuchs, E. C.; Gatterer, K.; Holler, G.; Woisetschlager, J. Dynamics of the Floating Water Bridge. *J. Phys. D. Appl. Phys.***2008** , *41* (18), 2–7. https://doi.org/10.1088/0022-3727/41/18/185502.

(91) Fuchs, E. C.; Woisetschlager, J.; Gatterer, K.; Maier, E.; Pecnik, R.; Holler, G.; Eisenkolbl, H. The Floating Water Bridge. *J. Phys. D. Appl. Phys.* **2007** , *40* (19), 6112–6114. https://doi.org/10.1088/0022-3727/40/19/052.

(92) Ponterio, R. C.; Pochylski, M.; Aliotta, F.; Vasi, C.; Fontanella, M. E.; Saija, F. Raman Scattering Measurements on a Floating Water Bridge. *J. Phys. D. Appl. Phys.* **2010** , *43* (17). https://doi.org/10.1088/0022-3727/43/17/175405.

(93) Chen, J.; Wang, C.; Wei, N.; Wan, R.; Gao, Y. 3D Flexible Water Channel: Stretchability of Nanoscale Water Bridge. *Nanoscale***2016** , *8* (10), 5676–5681. https://doi.org/10.1039/c5nr08072j.

(94) Bueno-Barrachina, J. M.; Canas-Penuelas, C. S.; Catalan-Izquierdo, S. Capacitance Evaluation on Non-Parallel Thick-Plate Capacitors by Means of Finite Element Analysis. *J. Energy Power Eng.***2011** , *5* , 373–378.

(95) Liu, N.; Zhang, R.; Li, Y.; Chen, B. Local Electric Field Effect of TMI (Fe, Co, Cu)-BEA on N2O Direct Dissociation. *J. Phys. Chem. C***2014** , *118* (20), 10944–10956. https://doi.org/10.1021/jp5023949.

(96) Chen, D.; Savidge, T. Comment on "Extreme Electric Fields Power Catalysis in the Active Site of Ketosteroid Isomerase." *Science (80-.).* **2015** , *349* (6251), 936b. https://doi.org/10.1126/science.aab0095.

(97) Barrachin, B.; Cohen de Lara, E. Determination of the Electric Field in Zeolites NaA, NaCaA and Ca6A. *J. Chem. Soc., Faraday Trans. 2* **1986** , *82* , 1953–1966.

(98) Skinner, L. B.; Benmore, C. J.; Shyam, B.; Weber, J. K. R.; Parise, J. B. Structure of the Floating Water Bridge and Water in an Electric Field. *Proc. Natl. Acad. Sci. U. S. A.* **2012** , *109*(41), 16463–16468. https://doi.org/10.1073/pnas.1210732109.

(99) Cramer, T.; Zerbetto, F.; Garcia, R. Molecular Mechanism of Water Bridge Buildup: Field-Induced Formation of Nanoscale Menisci.*Langmuir* **2008** , *24* (12), 6116–6120. https://doi.org/10.1021/la800220r.

(100) Hansen, J. S.; Todd, B. D.; Daivis, P. J. Prediction of Fluid Velocity Slip at Solid Surfaces. *Phys. Rev. E - Stat. Nonlinear, Soft Matter Phys.* **2011** , *84* (1), 1–8. https://doi.org/10.1103/PhysRevE.84.016313.

(101) Ferrari, L.; Kaufmann, J.; Winnefeld, F.; Plank, J. Interaction of Cement Model Systems with Superplasticizers Investigated by Atomic Force Microscopy, Zeta Potential, and Adsorption Measurements. *J. Colloid Interface Sci.* **2010** , *347* (1), 15–24. https://doi.org/10.1016/j.jcis.2010.03.005.

(102) Huber, F.; Berwanger, J.; Polesya, S.; Mankovsky, S.; Ebert, H.; Giessibl, F. J. Chemical Bond Formation Showing a Transition from Physisorption to Chemisorption. *Science (80-.).* **2019** ,*3444* (September), eaay3444. https://doi.org/10.1126/science.aay3444.

(103) Autumn, K.; Sitti, M.; Liang, Y. A.; Peattie, A. M.; Hansen, W. R.; Sponberg, S.; Kenny, T. W.; Fearing, R.; Israelachvili, J. N.; Full, R. J. Evidence for van Der Waals Adhesion in Gecko Setae. *Proc. Natl. Acad. Sci. U. S. A.* **2002** , *99* (19), 12252–12256. https://doi.org/10.1073/pnas.192252799.